High precision source characterization of intermediate mass-ratio black hole coalescences with gravitational waves: The importance of higher order multipoles

Tousif Islam,[1,2,3,4,*] Scott E. Field,[2,3] Carl-Johan Haster,[5,6] and Rory Smith[7,8]

[1]*Department of Physics, University of Massachusetts, Dartmouth, Massachusetts 02747, USA*
[2]*Department of Mathematics, University of Massachusetts, Dartmouth, Massachusetts 02747, USA*
[3]*Center for Scientific Computing and Visualization Research, University of Massachusetts, Dartmouth, Massachusetts 02747, USA*
[4]*Kavli Institute for Theoretical Physics, University of California, Santa Barbara, California 93106, USA*
[5]*LIGO Laboratory, Massachusetts Institute of Technology, 185 Albany Street, Cambridge, Massachusetts 02139, USA*
[6]*Department of Physics and Kavli Institute for Astrophysics and Space Research, Massachusetts Institute of Technology, 77 Massachusetts Avenue, Cambridge, Massachusetts 02139, USA*
[7]*School of Physics and Astronomy, Monash University, Melbourne VIC 3800, Australia*
[8]*OzGrav: The ARC Centre of Excellence for Gravitational Wave Discovery, Clayton VIC 3800, Australia*

(Received 14 May 2021; accepted 8 September 2021; published 19 October 2021)

Intermediate mass-ratio inspiral (IMRI) binaries—containing stellar-mass black holes coalescing into intermediate-mass black holes ($M > 100\ M_\odot$)—are a highly anticipated source of gravitational waves (GWs) for Advanced LIGO/Virgo. Their detection and source characterization would provide a unique probe of strong-field gravity and stellar evolution. Because of the asymmetric component masses and the large primary, these systems generically excite subdominant modes while reducing the importance of the dominant quadrupole mode. Including higher order harmonics can also result in a 10%–25% increase in signal-to-noise ratio for IMRIs, which may help to detect these systems. We show that by including subdominant gravitational-wave modes into the analysis we can achieve a precise characterization of IMRI source properties. For example, we find that the source properties for IMRIs can be measured to within 2%–15% accuracy at a fiducial signal-to-noise ratio of 25 if subdominant modes are included. When subdominant modes are neglected, the accuracy degrades to 9%–44% and significant biases are seen in chirp mass, mass ratio, primary spin, and luminosity distances. We further demonstrate that including subdominant modes in the waveform model can enable an informative measurement of both individual spin components and improve the source localization by a factor of ∼10. We discuss some important astrophysical implications of high precision source characterization enabled by subdominant modes such as constraining the mass gap and probing formation channels.

DOI: 10.1103/PhysRevD.104.084068

I. INTRODUCTION

Binaries consisting of a stellar-mass black hole and an intermediate-mass black hole (IMBH)—total mass $M \sim \mathcal{O}(10^2\ M_\odot)$—are a possible source of gravitational waves (GWs) for the current generation of detectors: Advanced LIGO [1], Virgo [2], and KAGRA [3]. Such sources are typically referred to as *intermediate mass-ratio inspirals* (IMRIs).[1] Detection of GWs from IMRIs will shed light on many interesting scientific questions [4–6]: IMRI sources will help us understand the formation channel and evolutionary pathway to supermassive black hole binaries [7] and probe stellar evolution [8], and investigate possible environmental effects of matter in the GW signal [4,9–15]. IMRI signals could further be used to test general relativity in the strong-field regime [16–22] and to offer an independent measurement of the Hubble constant [23].

Detectability and parameter estimation accuracy for IMRIs have garnered a lot of interest over the last few years [8,24–30]. When formed through hierarchical mergers, IMRI systems will have a large total mass and large spin on the primary. As a motivating example, if a GW190521-like remnant [31] ($M \approx 142\ M_\odot$, $\chi \approx .7$, $z \approx 0.8$) captured a $30\ M_\odot$ stellar-mass BH, the nascent IMRI system would have a detector-frame total mass of around $310\ M_\odot$. Because of the large total mass characterized by these systems, the

*tislam@umassd.edu

[1]We note that the merger and ringdown, in addition to the inspiral, are important for detection and source-parameter inference.

number of in-band inspiral cycles from the dominant quadrupole mode is negligible. Previous studies have shown that parameter inference using only the dominant quadrupole mode leads to large uncertainty and significant biases in key source parameters such as the mass and spin of the primary BH [27] and can potentially bias tests of GR [32]. This greatly reduces the science that can be extracted from IMRI signals, such as measuring the pair-instability mass gap [33–36], distinguishing between IMRI formation channels [4,5], and self-consistency tests of GR that will be especially informative given the unique IMRI signal [16–22].

Fortunately, the asymmetric black hole masses will excite subdominant modes that, due to their higher-frequency content, are in-band longer. In this paper, we show that including higher order harmonics into the parameter estimation analysis results in a 3 to 4 times improvement in the measurement uncertainties and 10 times improvement in the recovered 3D comoving volume that contains the true position of the binary. We further show that omission of higher order multipoles leads to either poorer constraints or completely biased estimation of binary properties. We focus on IMRIs with detector-frame total masses $175\,M_\odot < M < 300\,M_\odot$ and mass ratio $1/40 < q < 1/10$ ($q \coloneqq m_2/m_1$ with $m_1 \geq m_2$ and where m_1 and m_2 are the mass of the primary and secondary black holes, respectively). We also demonstrate that high precision parameter estimates are similarly obtained for generic-spin configurations and possible binaries in the pair-instability mass gap.

The rest of the paper is organized as the follows. Section II presents a brief outline of the data analysis framework. In Sec. III, we consider the detectability of IMRIs based on a signal-to-noise (SNR) computation. Parameter estimation results, the main contribution of this paper, is presented in Sec. IV. The robustness of our results is further discussed in Sec. V. Finally, we discuss the implications, caveats, and conclusions of our analysis in Sec. VI.

II. ANALYSIS SETUP

We model the strain data d from a GW detector as a gravitational-wave signal h with an added stream of random noise $n(t)$, often assumed to be Gaussian and stationary [37],

$$d(t) = h(t;\boldsymbol{\theta}) + n(t). \tag{1}$$

The gravitational-wave source parameters $\boldsymbol{\theta}$ can be inferred from the time-series data using Bayesian inference. Bayesian inference relates the probability of model parameters $\boldsymbol{\theta}$ to experimental data d, and a hypothesis for the data $\mathcal{H}$, via the Bayes theorem:

$$p(\boldsymbol{\theta}|d,\mathcal{H}) = \frac{\pi(\boldsymbol{\theta}|\mathcal{H})\mathcal{L}(d|\boldsymbol{\theta},\mathcal{H})}{\mathcal{Z}(d|\mathcal{H})}. \tag{2}$$

The quantity $p(\boldsymbol{\theta}|d,\mathcal{H})$ is the *posterior probability density* of the parameters $\boldsymbol{\theta}$ given d and $\mathcal{H}$; $\mathcal{L}(d|\boldsymbol{\theta},\mathcal{H})$ is the *likelihood* of d given $\boldsymbol{\theta}$ and $\mathcal{H}$; $\pi(\boldsymbol{\theta}|\mathcal{H})$ is the *prior* probability of $\boldsymbol{\theta}$; and $\mathcal{Z}(d|\mathcal{H})$ is the *evidence* (marginalized likelihood) of d given $\mathcal{H}$. The posterior density is the target for *parameter estimation* (PF), while the evidence is the target for *hypothesis testing*.

The vector, $\boldsymbol{\theta} = (\alpha, \delta, \psi, t_c, d_L, \mathbf{n}, \boldsymbol{\lambda})$ is a set of 15 parameters that completely characterizes a binary black hole GW signal in general relativity. The vector $\boldsymbol{\lambda} \coloneqq \{m_1, m_2, \chi_1, \chi_2, \theta_1, \theta_2, \phi_{12}, \phi_{jl}\}$ are the intrinsic parameters that describe the binary: the component masses m_1 and m_2 (with $m_1 > m_2$), dimensionless spin magnitudes χ_1 and χ_2, and four angles $\{\theta_1, \theta_2, \phi_{12}, \phi_{jl}\}$ describing the spin orientation (cf. Appendix of [38] for definitions of these angles), and d_L is the luminosity distance. The vector $\mathbf{n} \coloneqq \{\iota, \varphi_c\}$ is the direction of radiation in the source frame: ι is the inclination angle between the orbital angular momentum of the binary and line of sight to the observer, and φ_c and t_c are, respectively, the azimuthal angle and time at coalescence. Right ascension α and declination δ are the sky localization parameters whereas ψ is the polarization angle.

We consider a network of three ground-based detectors: two Advanced LIGO detectors and the Advanced Virgo detector, all operating at their respective design sensitivities [1,39] and use a zero noise configuration. Specifically, the synthetic detector data is exactly equal to the expected response due to our GW source. Since detector noise is assumed to be colored Gaussian noise with zero mean, this choice makes our analysis equivalent to an average over an ensemble of analyses which use infinitely many noise realizations [40]. To estimate the PDFs of BBH parameters $p(\boldsymbol{\theta}|d,H)$, we use the Bayesian inference package PARALLEL-BILBY[2] [38,41,42] with the DYNESTY [43] sampler. We consider binaries with total masses $175\,M_\odot \leq M \leq 300\,M_\odot$ and mass ratio $1/40 \leq q \leq 1/10$, which would merge in LIGO/Virgo's sensitive band [44].

We begin by considering binaries whose component spins are either aligned/antialigned with the orbital angular momentum. We employ the GW signal model `IMRPhenomPXHM` [45,46].[3] a state-of-the-art phenomenological nonprecessing multimode frequency-domain model, from the LALSuite software library [47]. The model includes $\{\ell, m\} = \{(2,\pm1), (3,\pm3), (3,\pm2), (4,\pm4)\}$ modes in addition to the dominant $\{\ell, m\} = (2,\pm2)$ quadrupolar mode. To demonstrate the validity of our results for generic-spin cases, we use IMRPhenomXPHM [48], a precessing extension of IMRPhenomXHM, that models GW signal emitted by quasicircular precessing BBHs.

We choose uniform priors for chirp masses $(5\,M_\odot < \mathcal{M}_c < 80\,M_\odot)$ and mass ratio $(1/150 < q < 1)$, defined in the detector frame. Unless otherwise specified, mass

[2]We use BILBY 1.0.3 and PARALLEL-BILBY 0.1.6.

[3]The model `IMRPhenomPXHM` has been generated with LALSuite version 6.79, while for analysis using the `IMRPhenomPXHM` model use LALSuite version 6.83.

parameters in this paper are always reported in the detector frame. This particular choice is made as the detector-frame masses are the directly observed quantities whereas source-frame masses are inferred using the estimated luminosity distance d_L. This introduces additional uncertainties in the inferred source-frame masses. For the component dimensionless spins, we use aligned-spin priors [49]. The prior on the luminosity distance is taken to be $P(d_L) \propto d_L^2$, with $20 \leq d_L \leq 3000$ Mpc. For the orbital inclination angle ι, we assume a uniform prior over $-1 \leq \cos\iota \leq 1$. Priors on the sky location parameters α and δ are assumed to be uniform over the sky with periodic boundary conditions.

III. DETECTABILITY OF HIGH MASS-RATIO MASSIVE BINARIES

To assess the detectability of the IMRIs in current-generation detectors [24,50], we generate signals using IMRPhenomXHM and compute the optimal network SNR [51] ρ at different points of the parameter space. In general, a network SNR of 8 to 10 is often sufficient for the detection of a GW signal. However, the statistical significance of a detection at a given SNR is established empirically [52]. In Fig. 1, we show the ratio of the optimal SNR of only the dominant $(\ell, m) = (2, \pm 2)$ mode and including the higher order modes as a function of total mass of the binary M for different mass ratios q. We find a significant SNR loss (10% to 25%) when disregarding the higher order modes, where a $(\ell, m) = (2, \pm 2)$-only analysis would be likely to miss otherwise clear detections of IMRIs. If the detector noise were truly Gaussian, this SNR loss corresponds to a reduction in the volume of the Universe (which is roughly $\sim\rho^3$) from which clear detections can be made of the order of 30%–60%. Because of non-Gaussian detector glitches, however, the sensitivity is likely to be degraded. Therefore, IMRIs are at present difficult to detect with template-based searches [53]. We further note that the SNR in both the dominant $(\ell, m) = (2, \pm 2)$ mode and in higher order modes are significantly greater than the detection threshold of ∼8–10 for the binaries we consider in this work and so may be detected with other methods [54,55]. The inclusion of higher order modes in modeled GW search pipelines is outside the scope of this paper but would warrant further explorations (see also [56] for effects on a more equal-mass BBH search).

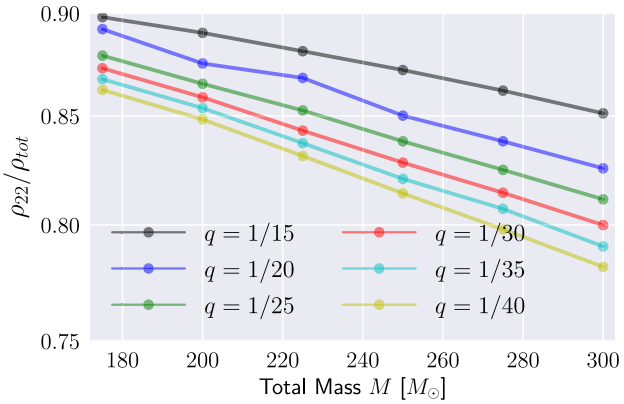

FIG. 1. Ratio of the optimal SNRs of only the $(2, \pm 2)$ modes, ρ_{22}, and all available modes, $\rho_{\rm tot}$, for binaries with total masses $175\ M_\odot < M < 300\ M_\odot$ and mass ratio $1/40 < q < 1/15$. We fix $d_L = 750$ Mpc, $\iota = 3\pi/4$, $\varphi_c = 3\pi/4$, $\alpha = 1.0$, $\delta = 1.0$, $\psi = 0.0$ and $t_c = 0.0$h Greenwich mean sidereal time (SNR as a function of ι, φ_c, and ψ is shown in Fig. 2).

A. SNR variation with source orientation

For all of our simulated events, we fix the inclination angle $\iota = 2.35$, azimuthal angle $\varphi = 2.35$, and polarization angle $\psi = 0.0$. Varying these values can raise or lower the

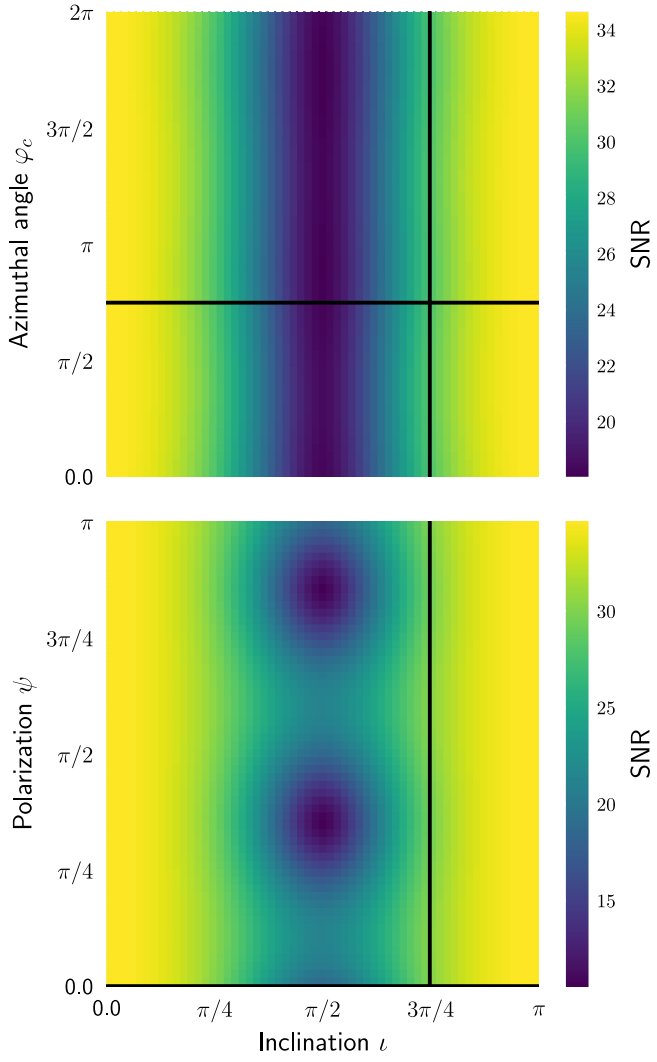

FIG. 2. SNR as a function of inclination angle ι, azimuthal angle φ_c and polarization ψ. We set $q = 30$, $M = 225\ M_\odot$, $\{\chi_1, \chi_2\} = \{0.6, 0.7\}$, $d_L = 750$ Mpc, $\alpha = 1.0$, and $\delta = 1.0$. Solid black lines indicate our choice of $\iota = 2.35$, $\varphi = 2.35$ and $\psi = 0.0$ for all of our injections.

SNR as the different harmonic modes can undergo constructive or destructive interference. In Fig. 2, we pick up a representative case of mass ratio $q = 30$ and show the SNR as a function of ι, φ, and ψ while keeping other parameters fixed. We set the total mass $M = 225\ M_\odot$, spins $\{\chi_1, \chi_2\} = \{0.6, 0.7\}$, luminosity distance $d_L = 750$ Mpc, right accession $\alpha = 1.0$, and declination $\delta = 1.0$. Our choice of $\iota(= 2.35)$, $\varphi(= 2.35)$, and $\psi(= 0.0)$ (black lines) for the simulated events fits in between optimal and conservative SNR expectations.

IV. PARAMETER ESTIMATION RESULTS

We now investigate the precision with which current-generation detectors will be able to measure the source properties of the IMRIs. We study the effects of higher order modes in parameter estimation and explore the validity of our results for binaries with generic spins, as well as special cases, e.g., face-on/off binaries.

A. Simulated GW signals

We employ IMRPhenomXHM to simulate the following sets of aligned-spin IMRI signals:

(i) **Set-M:** We fix $q = 1/30$, $\chi_1 = 0.6$, and $\chi_2 = 0.7$ while varying the total mass $M = \{175, 200, 225, 250, 275, 300\} M_\odot$. This set of spins matches with the predicted spin magnitudes of black holes formed through hierarchical mergers [57–59].

(ii) **Set-q:** We fix $M = 225\ M_\odot, \chi_1 = 0.6$, and $\chi_2 = 0.7$ while varying the mass ratio $q = \{1/40, 1/30, 1/20, 1/10\}$.

(iii) **Set-χ_1:** We fix $M = 225\ M_\odot$, $\chi_2 = 0.7$, and $q = 1/30$ while varying the dimensionless spin magnitude on the primary black hole $\chi_1 = \{-0.6, -0.3, 0.0, 0.3, 0.6\}$.

(iv) **Set-χ_2:** We fix $M = 225\ M_\odot$, $q = 1/30$, and $\chi_1 = 0.6$ while varying the dimensionless spin magnitude on the secondary black hole $\chi_2 = \{-0.7, -0.3, 0.0, 0.3, 0.7\}$.

For each binary, we set $\iota = 3\pi/4$, $\varphi_c = 3\pi/4$, $\alpha = 1.0$, $\delta = 1.0$ and $\psi = 0.0$ radians respectively. We further fix $t_c = 0.0$h Greenwich mean sidereal time. The distance to each source is then scaled so that the network SNR is $\rho = 25$ to ensure a fair comparison of PE accuracy across the parameter space. We use the same waveform model for injection and recovery thereby removing possible biases due to the choice of a particular waveform approximant [27,50,60]. We demonstrate the robustness of our results with respect to waveform model in Sec. V. For each simulated IMRI, we recover the source parameters with two different mode configurations: one with only the dominant $(\ell, m) = (2, \pm 2)$ modes and then with all available modes included. The injected signal, however, always contains all available modes.

B. Parameter estimation accuracy

In Fig. 3, we show the recovered 90% credible intervals for five important binary source properties: chirp mass $\mathcal{M}_c$, mass of the primary black hole m_1, mass ratio q, spin magnitudes χ_1, and luminosity distance d_L as a function of the injected total mass $M_{\rm inj}$, mass ratio $q_{\rm inj}$ and primary spin $\chi_{1,\rm inj}$. Similar to [27], we find that the best constrained parameters are chirp mass $\mathcal{M}_c$, mass ratio q, and spin on the primary black hole χ_1. The measurement accuracy of $\mathcal{M}_c$ depends on the number of in-band inspiral cycles. As the total mass of the binary increases, the observable signal becomes dominated by the merger and ringdown part. Therefore, the uncertainty on $\mathcal{M}_c$ is expected to increase with increasing M. We find that $\mathcal{M}_c$ can be measured with an accuracy of $\sim$3% for a binary with total mass $M = 175\ M_\odot$ (and $q = 1/30$) while the uncertainty increases to $\sim$7% for $M = 300\ M_\odot$ (and $q = 1/30$). In Table I, we summarize the uncertainties on $\mathcal{M}_c$, m_1, q, χ_1, and d_L along with the biases in estimation for binaries at the boundary of our parameter space. Since we are using zero noise, our results are equivalent to ensemble averages. This implies that the bias parameter $\beta_\theta = \theta_{\rm true} - \theta_{\rm recovered}$ (where $\theta_{\rm true}$ is the true value of the parameter and $\theta_{\rm recovered}$ is the median of the recovered posterior for θ) is, in some sense, the exact quantification of bias from the injected value. For typical systems, m_1, q, and χ_1 are well constrained with $\sim$10% of accuracy when higher modes are included. Relative errors on M $(\chi_{\rm eff})$ closely follow that of m_1 (χ_1) (cf. Figs. 3 and 4). As the binary becomes more asymmetric, the number of waveform cycles in the detector band increases, resulting in a decrease in measurement uncertainties of q. Uncertainties in d_L are typically $\sim$20%. When all other parameters are fixed, a negative spin on the primary black hole reduces the number of in-band cycles in the gravitational waveform, implying a severe loss of information in the detected signal. This leads to significant increase in uncertainties on almost all the recovered parameters for the binary with $\{M, q, \chi_1, \chi_2\} = \{225\ M_\odot, 1/30, -0.6, +0.7\}$.

C. Constraints on total mass M and effective spin $\chi_{\rm eff}$

We compute the dimensionless 90% credible uncertainties for the total mass of the binary, M, and the effective inspiral spin, $\chi_{\rm eff}$. We find that, due to the smaller black hole being well approximated by the structureless point particle, the relative errors on M $(\chi_{\rm eff})$ closely follow that of m_1 (χ_1). In Fig. 4 and 5, we show the 90% uncertainties for different parameters as a function of the injected total mass (BBH configurations set-M) and mass ratio (BBH configurations set-q).

D. Measureability of Spin Magnitudes

We now consider individual spin measurements for IMRIs, using an aligned-spin prior (solid blue lines) for

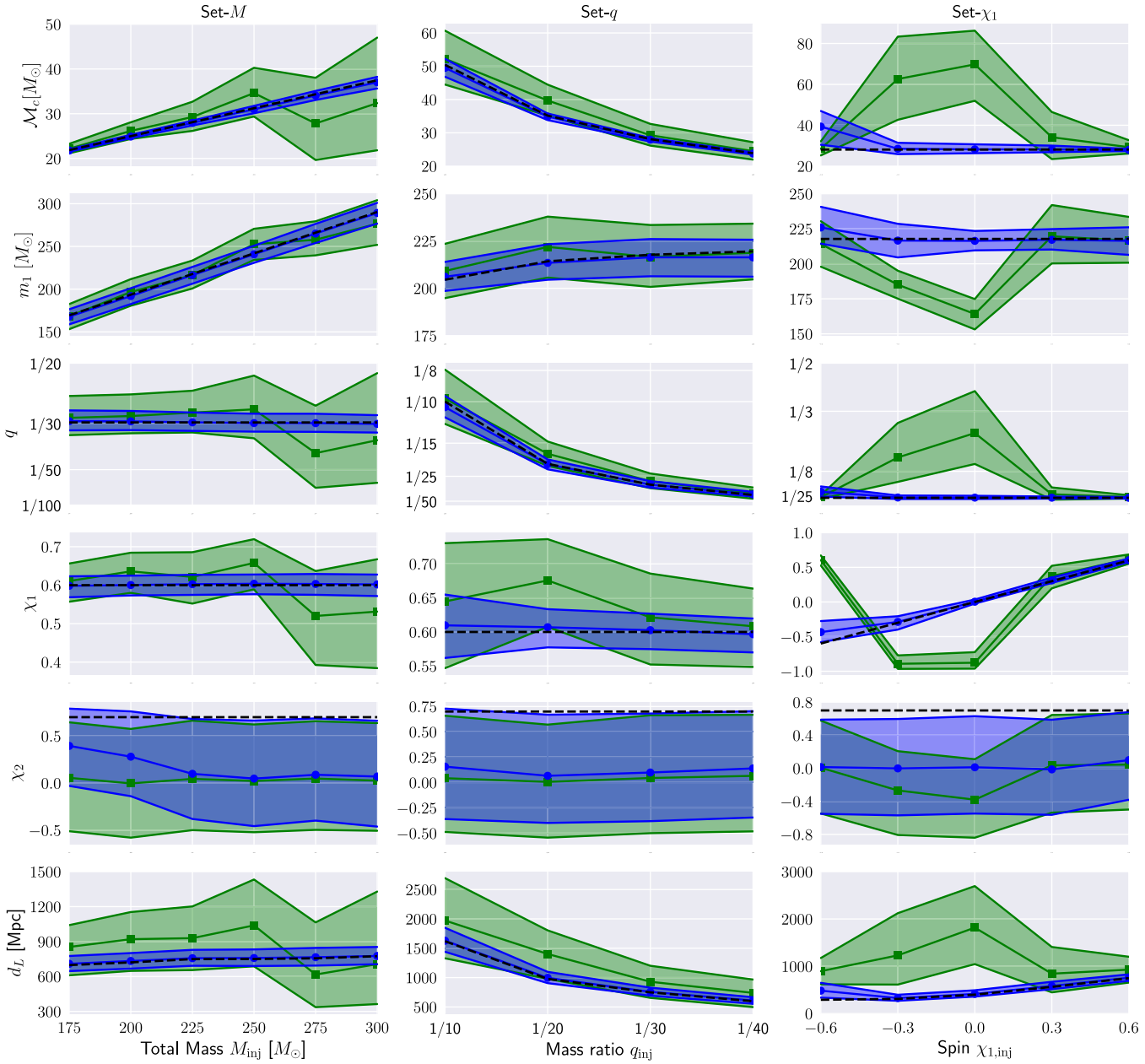

FIG. 3. The 90% credible interval for the total mass of the binary M, mass of the primary black hole m_1, mass ratio q, dimensionless spin parameters χ_1 and χ_2, and luminosity distance d_L as a function of the injected total mass $M_{\rm inj}$ (left panels), injected mass ratio $q_{\rm inj}$ (middle panels), and injected spin magnitude on the primary black hole $\chi_{1,\rm inj}$ (right panels). 90% credible interval for the $(2,\pm2)$ mode (all modes) recovery is shown in green (blue) and the true values are plotted as a dashed black line. Columns 1, 2, and 3 correspond to BBH configurations of set-M, set-q, and set-χ_1, respectively.

the both spins. While χ_1 can be precisely measured for most of the binaries (as seen in Fig. 3), the spin on the secondary black hole χ_2 generally remains uninformative. However, contrary to our general expectation, we find that one may be able to constraint χ_2 due to the presence of higher modes. We find that the 90% credible intervals for χ_2 may be reasonably resolved for our binaries with masses $M < 225\ M_\odot$. For larger total masses, the number of resolvable inspiral cycles reduces drastically, implying a sharp drop in available information in the detected signal. In Fig. 6, we show the χ_2 posteriors recovered with only $(2,\pm2)$ modes (black dashed lines) and with all modes (green solid lines) for the injections created in set $-$ M with varying total masses. It shows that while the $(2,\pm2)$ mode recovery cannot constrain χ_2, this parameter can be measured when the recovery model includes higher order modes and the signal contains a sufficient number of resolvable inspiral cycles.

TABLE I. Parameter estimation accuracy for the binaries used in our analysis.[a] We report the dimensionless uncertainties $\Delta\theta/\theta_{\rm inj}$ and biases β_θ for five representative parameters. Symbols: $\mathcal{M}_c$: detector-frame chirp mass; q: mass ratio; χ_1: dimensionless spin on the primary black hole; V_{22} and V_{hm} are the recovered 90% credible region of the comoving volume (computed using ligo − skymap) containing the true position of the binary with and without the higher modes, respectively. The bias in parameter λ computed as $\beta_\theta = |\theta_{\rm true} - \theta_{\rm recovered}|$, where $\theta_{\rm true}$ is the true value of the parameter and $\theta_{\rm recovered}$ is the median of the recovered posterior for θ. Values in parenthesis denote uncertainties and biases when only the $(2, \pm 2)$ mode is used in the recovery model.

Binaries	$\frac{\Delta\theta}{\theta_{\rm inj}}$ (%)					Biases					
$\{\mathcal{M}_c, m_1, 1/q, \chi_1, \chi_2, d_L\}$	$\frac{\Delta\mathcal{M}_c}{\mathcal{M}_{c,\rm inj}}$	$\frac{\Delta m_1}{m_{1,\rm inj}}$	$\frac{\Delta 1/q}{1/q_{\rm inj}}$	$\frac{\Delta\chi_1}{\chi_{1,\rm inj}}$	$\frac{\Delta d_L}{d_{L,\rm inj}}$	$\beta_{\mathcal{M}_c}$	β_{m_1}	$\beta_{1/q}$	β_{χ_1}	β_{d_L}	$\frac{V_{22}}{V_{hm}}$
Set-M											
$\{21.86, 169.35, 30, +0.6, +0.7, 697.84\}$	2.3	10.3	16.9	9.0	18.6	0.077	1.540	0.32	0.0015	10.99	9.32
	(9.6)	(17.1)	(33.1)	(16.5)	(61.7)	(0.326)	(1.13)	(1.13)	(0.0108)	(155.6)	
$\{24.98, 193.54, 30, +0.6, +0.7, 720.69\}$	3.0	9.5	16.2	8.5	18.5	0.086	1.601	0.28	0.0004	12.43	11.12
	(14.9)	(16.1)	(32.9)	(17.4)	(70.1)	(1.169)	(3.087)	(1.54)	(0.0359)	(199.4)	
$\{28.11, 217.74, 30, +0.6, +0.7, 749.13\}$	3.8	9.0	15.5	8.6	18.2	0.1641	1.467	0.02	0.0026	7.89	13.06
	(23.1)	(14.9)	(35.3)	(22.3)	(72.9)	(1.167)	(1.254)	(2.31)	(0.0214)	(179.8)	
$\{31.23, 241.93, 30, +0.6, +0.7, 750.10\}$	5.3	8.3	15.2	8.5	18.9	0.236	1.167	0.15	0.0036	8.35	24.80
	(34.8)	(15.1)	(53.1)	(21.7)	(99.4)	(3.386)	(10.591)	(3.00)	(0.0578)	(288.6)	
$\{34.35, 266.13, 30, +0.6, +0.7, 756.02\}$	5.9	8.4	15.3	9.0	20.0	0.282	1.067	0.17	0.0031	9.40	7.36
	(53.4)	(15.0)	(69.4)	(40.7)	(96.3)	(6.524)	(8.363)	(10.53)	(0.0800)	(139.4)	
$\{37.47, 290.32, 30, +0.6, +0.7, 774.01\}$	6.9	8.3	14.7	9.3	19.1	0.454	1.327	0.36	0.0020	1.99	13.81
	(67.2)	(18.0)	(92.8)	(47.2)	(124.8)	(5.108)	(13.619)	(5.31)	(0.0686)	(68.2)	
Set-q											
$\{28.11,204.5,10,+0.6,+0.7,1620.1\}$	10.6	7.4	17.1	15.5	25.2	0.894	1.54	0.46	0.0097	8.31	9.29
	(14.1)	(43.5)	(30.6)	(84.2)	(11.3)	(1.836)	(4.59)	(0.23)	(0.044)	(351.8)	
$\{28.11, 214, 2, 20, +0.6, +0.7, 978.16\}$	5.6	8.7	15.8	9.3	19.6	0.287	0.80	0.13	0.0069	17.95	15.88
	(26.4)	(13.5)	(39.1)	(21.5)	(84.3)	(4.529)	(4.93)	(2.78)	(0.075)	(424.2)	
$\{28.11, 217.7, 30, +0.6, +0.7, 749.13\}$	3.8	9.0	15.5	8.6	18.2	0.164	1.46	0.03	0.0026	7.89	13.06
	(23.1)	(14.9)	(35.3)	(22.3)	(72.9)	(1.167)	(1.25)	(2.31)	(0.021)	(179.8)	
$\{28.11, 219.5, 40, +0.6, +0.7, 598.04\}$	2.8	8.9	15.2	8.3	18.5	0.101	3.24	0.66	0.0032	11.15	13.10
	(21.8)	(13.4)	(35.9)	(19.2)	(78.5)	(0.631)	(0.682)	(1.84)	(0.008)	(141.8)	
Set-χ_1											
$\{28.11, 217.7, 30, -0.6, +0.7, 292.01\}$	58.7	12.1	106.2	50.6	107.1	11.23	8.18	11.63	0.165	192.59	9.41
	(24.4)	(14.9)	(37.1)	(24.1)	(190.0)	(0.40)	(3.73)	(1.65)	(1.20)	(604.3)	
$\{28.11, 217.7, 30, -0.3, +0.7, 309.83\}$	19.7	11.0	36.6	64.1	40.9	0.39	1.07	0.9	0.012	17.72	215.33
	(144.7)	(9.1)	(613.7)	(64.7)	(487.2)	(34.50)	(32.79)	(24.25)	(0.59)	(920.6)	
$\{28.11, 217.7, 30, 0.0, +0.7, 400.15\}$	15.4	6.3	33.7	⋯	33.3	0.11	1.39	0.57	0.003	14.75	306.86
	(122.1)	(9.8)	(758.7)	⋯	(412.2)	(41.67)	(53.50)	(26.15)	(0.87)	(1416.8)	
$\{28.11, 217.7, 30, +0.3, +0.7, 564, 22\}$	11.3	6.7	21.6	25.8	27.6	0.07	0.66	0.36	0.011	18.91	22.26
	(81.9)	(19.1)	(127.6)	(108.6)	(170.1)	(6.04)	(1.89)	(8.04)	(0.08)	(279.1)	
$\{28.11, 217.7, 30, +0.6, +0.7, 759.13\}$	3.8	9.0	15.5	8.6	18.2	0.16	1.46	0.03	0.002	7.89	13.06
	(23.1)	(14.9)	(35.3)	(22.3)	(72.9)	(1.16)	(1.25)	(2.31)	(0.02)	(179.8)	
Set-χ_2											
$\{28.11, 217.7, 30, +0.6, -0.7, 736.13\}$	4.19	9.6	16.5	9.6	19.2	0.16	1.46	0.75	0.0093	18.32	10.97
	(27.0)	(15.5)	(40.4)	(25.9)	(80.4)	(0.94)	(5.94)	(2.91)	(0.005)	(182.5)	
$\{28.11, 217.7, 30, +0.6, -0.3, 742.08, \}$	4.18	9.6	16.2	9.6	18.3	0.08	1.38	0.52	0.0056	14.47	14.02
	(25.4)	(15.2)	(38.2)	(25.4)	(77.0)	(0.54)	(5.71)	(2.23)	(0.006)	(157.8)	
$\{28.11, 217.7, 30, +0.6, 0.0, 746.52, \}$	4.24	9.7	16.1	9.7	18.8	0.003	1.08	0.28	0.0021	11.80	11.41
	(24.3)	(15.0)	(37.8)	(24.2)	(74.3)	(0.12)	(5.16)	(1.48)	(0.007)	(131.3)	
$\{28.11, 217.7, 30, +0.6, +0.3, 751.19\}$	4.33	9.5	16.1	9.3	19.1	0.06	1.14	0.16	0.0001	10.77	10.09
	(24.8)	(15.1)	(36.9)	(24.1)	(76.5)	(0.38)	(3.87)	(1.58)	(0.002)	(139.7)	
$\{28.11, 217.7, 30, +0.6, +0.7, 759.13\}$	3.8	9.0	15.5	8.6	18.2	0.16	1.46	0.03	0.002	7.89	13.06
	(23.1)	(14.9)	(35.3)	(22.3)	(72.9)	(1.16)	(1.25)	(2.31)	(0.02)	(179.8)	

[a]The two missing entries for set-χ_1 corresponds to the cases where the injected value of $\chi_1 = 0.0$. Therefore, $\Delta\theta/\theta_{\rm inj}$ is undefined.

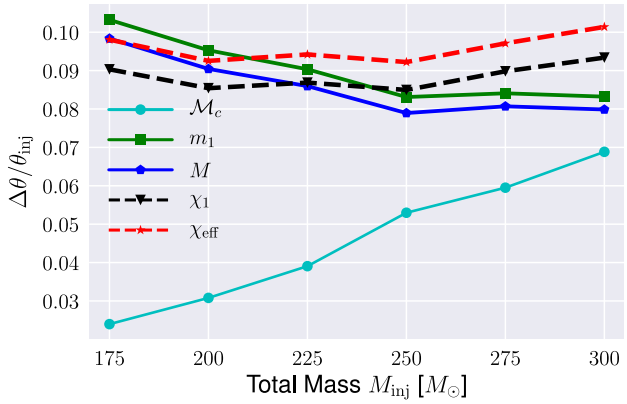

FIG. 4. Dimensionless 90% uncertainties $\Delta\theta/\theta_{\rm inj}(\%)$ for chirp mass $\mathcal{M}_c$, total mass M, mass of the primary black hole m_1, spin on the primary black hole χ_1, and effective inspiral spin $\chi_{\rm eff}$ as a function of the injected total mass (corresponding to BBH configurations set-M).

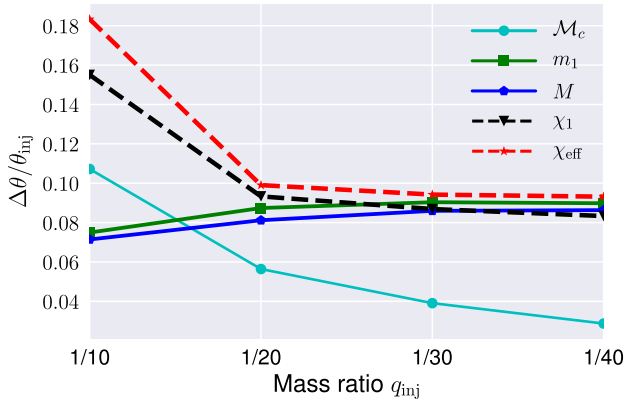

FIG. 5. Dimensionless 90% uncertainties $\Delta\theta/\theta_{\rm inj}(\%)$ for chirp mass $\mathcal{M}_c$, total mass M, mass of the primary black hole m_1, spin on the primary black hole χ_1, and effective inspiral spin $\chi_{\rm eff}$ as a function of the injected mass ratio (corresponding to BBH configurations set-q).

E. Importance of higher order modes

The impact of higher modes in detection and parameter estimation has been extensively studied in the comparable- to moderate-mass-ratio regime ($q \lesssim 8$) often using Fisher matrix-based studies or reanalyzing novel gravitational-wave events [56,61–73]. Our fully Bayesian results, which focus on plausible IMRI systems for the upcoming LIGO-Virgo-KAGRA observing run, are in broad agreement with these previous works: higher order modes are increasingly important as the value of the mass ratio increases and/or effective spin decreases, and recovery models that include all modes significantly reduce bias in all cases. As compared to previous IMRI studies using only the quadrupole mode [27], however, the extent to which higher order modes enable precise measurements of most system parameters is surprising. This is due to the unique ability of massive IMRIs to excite sufficiently loud higher order modes that lie in the detector's sensitive band.

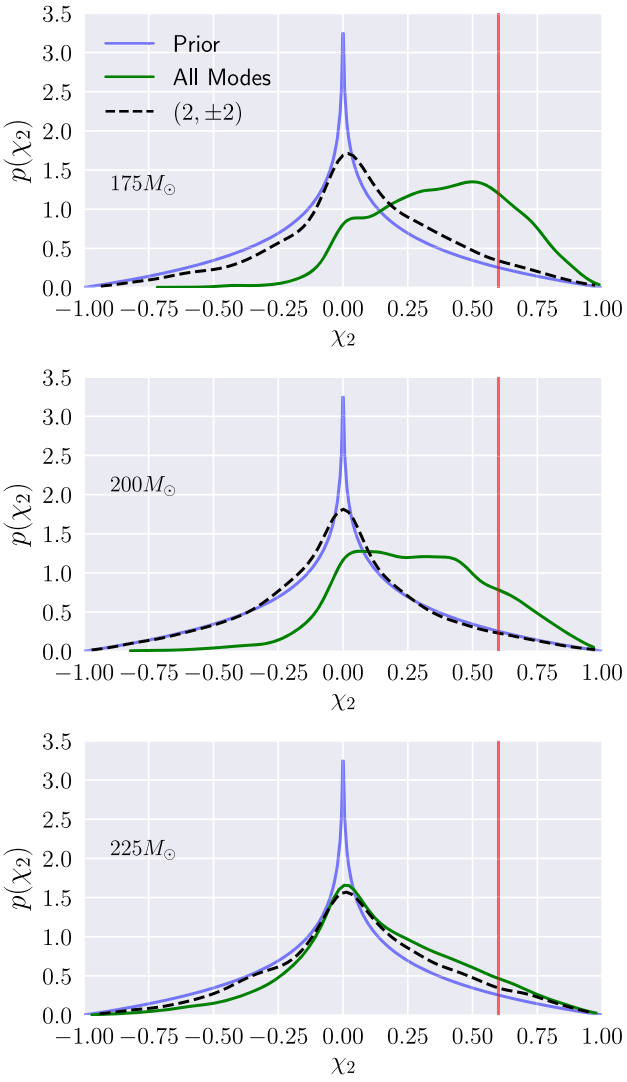

FIG. 6. Posterior for the secondary spin parameter χ_2 recovered with (solid green) and without the higher modes (dashed black) for binaries with varying total masses (**set-*M***) injections. Blue solid lines show aligned-spin prior [49]). All other parameters are set to the default values described in the text. Vertical red lines indicate the true value.

To probe the impact of these subdominant multipoles within our analysis setup, we recover the injected signal with (i) only $(2,\pm2)$ modes and (ii) with all available modes including the dominant $(2,\pm2)$ mode. We observe that (i) the 90% credible interval becomes significantly tighter when higher modes are included in recovery model and (ii) omission of higher modes results in substantial bias in parameter estimation for most binaries (cf. Table I and Fig. 3). For signals with varied primary spin (**set-χ_1**), we find significant bias whenever $\chi_{1,\rm inj} < 0.3$ with increasing bias as $\chi_{1,\rm inj}$ is lowered. While this effect is well known from comparable mass-ratio studies with negative

spin [61,62,73] (cf. Fig. 11 of Ref. [73]), what is particularly striking is that for massive IMRIs noticeable bias occurs even for positive spins as large as $\chi_{1,\mathrm{inj}} \approx 0.3$. We further find that, when higher modes are included, 90% credible region of the recovered comoving volume that contains the true position of the binary is shrunk by almost 10 times (Table I). Taken together, these results demonstrate that higher modes will play an especially central role in analyzing signals from high mass-ratio massive binaries, including source localization and precise estimation of source properties.

F. Face-off binaries

Nearly all gravitational-wave observations to date have been characterized by face-on (i.e., inclination angle $\iota = 0.0$) or face-off (i.e., inclination angle $\iota = \pi$) orientation to the line of sight [52], minimizing the possibility of detecting higher order modes in general. For such binaries, most of the higher order modes are expected to be weak. However, we show that, for massive high mass-ratio binaries, higher order modes may have sufficient SNRs such that they can no longer be disregarded even for face-on/face-off cases. To investigate that, we simulate a signal with total mass $M = 225\ M_\odot$, mass ratio $q = 1/30$, spins $\{\chi_1, \chi_2\} = \{0.6, 0.7\}$ in face-off orientation such that the SNR is 25. We then estimate the parameters using only the $(2, \pm 2)$ mode and with higher modes. In Fig. 7, we show the recovered posteriors with (solid green) and without (dashed black) the higher order modes. We find that including the higher order modes helps constrain the parameters better even for a face-off binary.

G. Generic-spin case

While our work has exclusively focused on the aligned-spin system, we now provide preliminary results for generic-spin binaries. In Fig. 8, we show two representative cases: we simulate signals with $\{M, q, \chi_1, \chi_2\} = \{225\ M_\odot, 1/30, 0.6, 0.7\}$ with aligned-spin and precessing spin configurations. For the generic-spin case, we choose the spin angles as

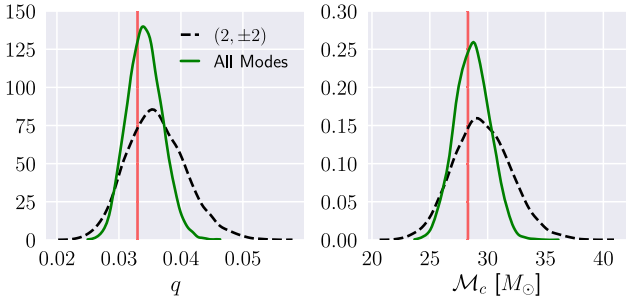

FIG. 7. Mass posteriors recovered with (solid green) and without the higher modes (dashed black) for the binary with $M = 225\ M_\odot$ and mass ratio $q = 1/30$ in a face-off configuration. Vertical lines show the true values. All other details are same as in Fig. 6.

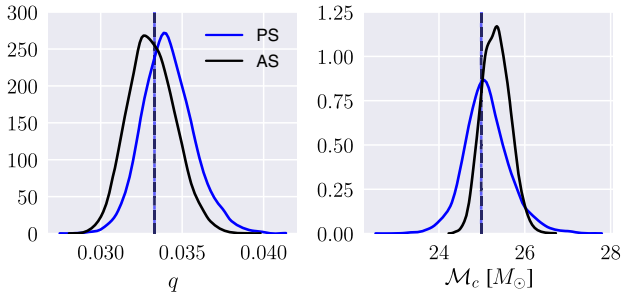

FIG. 8. Same as in Fig. 7 but for binaries with $M = 225\ M_\odot$, $q = 1/30$ in aligned spin (AS) and generically precessing spins (PS) configuration. Vertical lines show the true values.

$\theta_1 = 1.05$ and $\theta_2 = 1.02$, $\phi_{12} = 3.53$, and $\phi_{jl} = 3.75$, respectively (cf. the Appendix of [38]). The signal is then recovered with the generic-spin IMRPhenomXPHM model. We show the chirp mass and mass-ratio posteriors recovered for both the cases. We recover the mass source properties with similar accuracy. Future work should include a more comprehensive investigation of generic-spin IMRI systems.

H. Mass-gap binaries

Pair-instability and pulsational-pair-instability supernovae [74] prevent the formation of black holes with masses more than $\sim 50\ M_\odot$ from stellar collapse. This leads to a gap in the black-hole mass distribution function in between $\sim 50\ M_\odot$ and $\sim 130\ M_\odot$ [33–36]. The edges of the mass-gap region vary depending on the details of the pair-instability process, evolution of massive stars, and core-collapse supernova explosion [75,76]. However, multiple stellar mergers and the merger of black holes can lead to the formation of a black hole in the pair stability mass-gap region [77]. It is therefore an interesting question to ask whether our results are valid for binaries with at least one black hole that falls in the pair-instability mass gap. We simulate a signal with $\{M, q\} = \{120\ M_\odot, 1/10\}$ with a SNR of 25. The mass of the primary black hole is

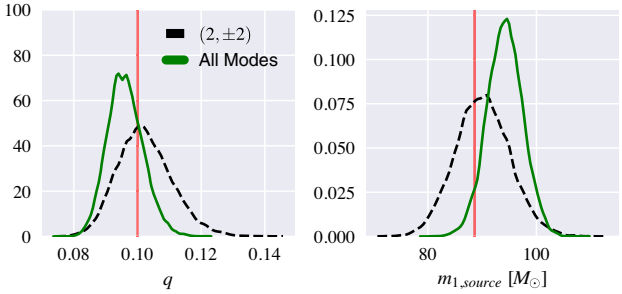

FIG. 9. Mass posteriors recovered with (solid green) and without the higher modes (dashed black) for the binary with $M = 120\ M_\odot$ and mass ratio $q = 1/10$. The source mass of the primary black hole lie in the pair-instability mass gap of $\sim 50\ M_\odot < M < 130\ M_\odot$. Vertical lines show the true values. All other details are same as in Fig. 6.

109.1 $M_\odot$ (88.35 $M_\odot$ in the source frame). All other parameters are fixed to the default values used in this paper. In Fig. 9, we show the recovered mass posteriors (in the source frame) with and without subdominant modes. 90% credible regions are tighter when higher-order multiples are included in the recovery model.

V. COMPARISON WITH SEOBNRV4HM_ROM RESULTS

Our parameter estimation results are obtained using IMRPhenomXHM [46], a frequency-domain phenomenological waveform model which is calibrated to numerical relativity waveforms in the comparable mass ratio regime ($q >= 1/18$) and to waveforms obtained from solving the perturbative Teukolsky equation for $1/1000 >= q >= 1/200$. As the model is uncalibrated in parts of the mass ratio regime we are looking at (i.e., $1/40 <= q <= 1/10$), we decide to redo the parameter estimation with a different waveform model for some of the representative cases. We choose the boundary cases in our parameter space (as listed in Table I) and employ SEOBNRv4HM_ROM [78], a reduced order based effective-one-body model, in both injection and recovery. We find that the measurement uncertainties in different parameters do not change significantly. As an example, in Fig. 10, we show the recovered posteriors for the chirp mass M_c and mass ratio q obtained using both IMRPhenomXHM and SEOBNRv4HM_ROM. As none of the models are calibrated to NR simulations, it is not possible to prefer the results obtained using one of the approximants over others. Further, systematic analysis involving different waveform models in injection and recovery is also beyond the scope of the current paper. However, we expect the general parameter estimation trends presented in the paper, which have been compiled with IMRPhenomXHM, to be applicable to other IMRI waveform models.

VI. CONCLUSION

High mass-ratio massive binaries consisting of a stellar-mass black hole and an IMBH, typically known as IMRIs, are a highly anticipated source of GWs for Advanced LIGO/Virgo. Because of the large total mass characterized by these systems, the number of in-band inspiral cycles (and therefore the power) from the dominant quadrupole mode is greatly reduced as compared to comparable mass binaries. In this paper, by focusing on aligned-spin systems with detector-frame total masses 175 $M_\odot < M < 300\ M_\odot$ and mass ratios $1/40 < q < 1/10$, we show that including higher order harmonics into the analysis (i) results in a 3 to 4 times improvement in the measurement uncertainties and (ii) 10 times improvement in the recovered 3D comoving volume that contains the true position of the binary, (iii) constrain the spin magnitude of the primary and secondary black hole better than previously expected, and (iv) may improve the detectability of such binaries significantly. We further show that current-generation detectors are able to estimate the source properties of such binaries with 1%–15% accuracy if higher order modes are included in the waveform model. Omitting higher order modes, on the other hand, results in catastrophic parameter bias for many binary systems. As one particularly striking

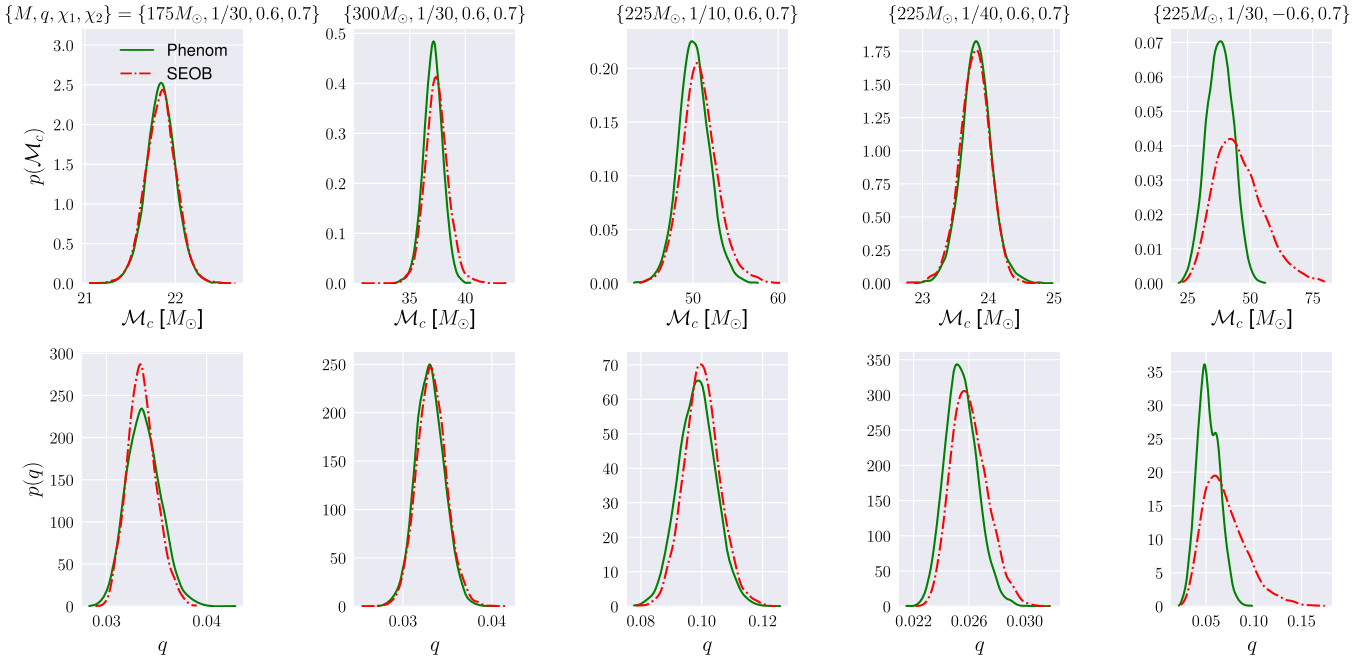

FIG. 10. Chirp mass and mass-ratio posteriors recovered with IMRPhenomXHM (solid green) and SEOBNRv4HM_ROM (dash dotted red) for the binaries in the boundary of our parameter space.

example, a binary black hole system with mass ratio of $q = 1/30$ and whose nonspinning primary BH has a mass of $m_1 = 218\ M_\odot$ is misclassified as a $q \sim 1/4$ system with $m_1 \sim 162\ M_\odot$ and $\chi_1 \sim -0.88$ (Fig. 3). These large parameter biases and measurement uncertainties would greatly reduces the science that can be extracted from IMRI signals, such as measuring the pair-instability mass gap [33–36], distinguishing between IMRI formation channels [4,5], and self-consistency tests of GR that will be especially informative given the unique IMRI signal [16–22]. We further discuss the robustness of our results with respect to waveform systematics, face-on binaries (which suppress higher order modes), generic orbits with misaligned spins, and special cases such as when one of the component black holes lies in the pair-instability mass gap ($\sim 50\ M_\odot < m_1 < 130\ M_\odot$) [33–36].

ACKNOWLEDGMENTS

We thank Christopher Berry, Juan Calderon Bustillo, Harald Pfeiffer, Geraint Pratten, and Gaurav Khanna for helpful discussions and feedback. T. I. is supported by NSF Grants No. PHY-1806665 and No. DMS-1912716, and a Doctoral Fellowship provided by UMassD Graduate Studies. S. E. F. is partially supported by NSF Grants No. PHY-1806665 and No. DMS-1912716. C.-J. H. acknowledges support of the National Science Foundation, and the LIGO Laboratory. LIGO was constructed by the California Institute of Technology and Massachusetts Institute of Technology with funding from the National Science Foundation and operates under cooperative agreement PHY-1764464. The computational work of this project was performed on the CARNiE cluster at UMassD, which is supported by the ONR/DURIP Grant No. N00014181255. A portion of this material is based upon work supported by the National Science Foundation under Grant No. DMS-1439786 while the author was in residence at the Institute for Computational and Experimental Research in Mathematics in Providence, RI, during the Advances in Computational Relativity program. This research was supported in part by the Heising-Simons Foundation, the Simons Foundation, and National Science Foundation Grant No. NSF PHY-1748958. This is LIGO Document Number DCC-P2100151.

[1] J. Aasi *et al.* (LIGO Scientific Collaboration), Classical Quantum Gravity **32**, 074001 (2015).
[2] F. Acernese *et al.* (VIRGO Collaboration), Classical Quantum Gravity **32**, 024001 (2015).
[3] T. Akutsu *et al.* (KAGRA Collaboration), arXiv:2005.05574.
[4] P. Amaro-Seoane, J. R. Gair, M. Freitag, M. Coleman Miller, I. Mandel, C. J. Cutler, and S. Babak, Classical Quantum Gravity **24**, R113 (2007).
[5] C. P. L. Berry, S. A. Hughes, C. F. Sopuerta, A. J. K. Chua, A. Heffernan, K. Holley-Bockelmann, D. P. Mihaylov, M. C. Miller, and A. Sesana, arXiv:1903.03686.
[6] M. A. Sedda *et al.*, Classical Quantum Gravity **37**, 215011 (2020).
[7] J. Bellovary, A. Brooks, M. Colpi, M. Eracleous, K. Holley-Bockelmann, A. Hornschemeier, L. Mayer, P. Natarajan, J. Slutsky, and M. Tremmel, arXiv:1903.08144.
[8] J. R. Gair, I. Mandel, M. C. Miller, and M. Volonteri, Gen. Relativ. Gravit. **43**, 485 (2011).
[9] E. Barausse, L. Rezzolla, D. Petroff, and M. Ansorg, Phys. Rev. D **75**, 064026 (2007).
[10] E. Barausse and L. Rezzolla, Phys. Rev. D **77**, 104027 (2008).
[11] J. R. Gair, E. E. Flanagan, S. Drasco, T. Hinderer, and S. Babak, Phys. Rev. D **83**, 044037 (2011).
[12] N. Yunes, B. Kocsis, A. Loeb, and Z. Haiman, Phys. Rev. Lett. **107**, 171103 (2011).
[13] E. Barausse, V. Cardoso, and P. Pani, Phys. Rev. D **89**, 104059 (2014).
[14] E. Barausse, V. Cardoso, and P. Pani, J. Phys. Conf. Ser. **610**, 012044 (2015).
[15] A. Derdzinski, D. D'Orazio, P. Duffell, Z. Haiman, and A. Macfadyen, Mon. Not. R. Astron. Soc. **501**, 3540 (2020).
[16] J. R. Gair, M. Vallisneri, S. L. Larson, and J. G. Baker, Living Rev. Relativity **16**, 7 (2013).
[17] G. A. Piovano, A. Maselli, and P. Pani, Phys. Lett. B **811**, 135860 (2020).
[18] N. Yunes and C. F. Sopuerta, J. Phys. Conf. Ser. **228**, 012051 (2010).
[19] P. Canizares, J. R. Gair, and C. F. Sopuerta, J. Phys. Conf. Ser. **363**, 012019 (2012).
[20] P. Canizares, J. R. Gair, and C. F. Sopuerta, Phys. Rev. D **86**, 044010 (2012).
[21] C. L. Rodriguez, I. Mandel, and J. R. Gair, Phys. Rev. D **85**, 062002 (2012).
[22] A. J. K. Chua, S. Hee, W. J. Handley, E. Higson, C. J. Moore, J. R. Gair, M. P. Hobson, and A. N. Lasenby, Mon. Not. R. Astron. Soc. **478**, 28 (2018).
[23] C. L. MacLeod and C. J. Hogan, Phys. Rev. D **77**, 043512 (2008).
[24] I. Mandel and J. R. Gair, Classical Quantum Gravity **26**, 094036 (2009).
[25] E. A. Huerta and J. R. Gair, Phys. Rev. D **83**, 044020 (2011).
[26] E. A. Huerta and J. R. Gair, Phys. Rev. D **83**, 044021 (2011).
[27] C.-J. Haster, Z. Wang, C. P. L. Berry, S. Stevenson, J. Veitch, and I. Mandel, Mon. Not. R. Astron. Soc. **457**, 4499 (2016).
[28] N. W. C. Leigh, N. Lützgendorf, A. M. Geller, T. J. Maccarone, C. Heinke, and A. Sesana, Mon. Not. R. Astron. Soc. **444**, 29 (2014).

[29] M. MacLeod, M. Trenti, and E. Ramirez-Ruiz, Astrophys. J. **819**, 70 (2016).
[30] P. Amaro-Seoane, Phys. Rev. D **98**, 063018 (2018).
[31] R. Abbott *et al.* (LIGO Scientific, Virgo Collaborations), Phys. Rev. Lett. **125**, 101102 (2020).
[32] P. T. H. Pang, J. Calderón Bustillo, Y. Wang, and T. G. F. Li, Phys. Rev. D **98**, 024019 (2018).
[33] K. Belczynski *et al.*, Astron. Astrophys. **594**, A97 (2016).
[34] M. Renzo, R. J. Farmer, S. Justham, S. E. de Mink, Y. Götberg, and P. Marchant, Mon. Not. R. Astron. Soc. **493**, 4333 (2020).
[35] R. Farmer, M. Renzo, S. E. de Mink, P. Marchant, and S. Justham, Astrophys. J. **887**, 53 (2019).
[36] S. Stevenson, M. Sampson, J. Powell, A. Vigna-Gómez, C. J. Neijssel, D. Szécsi, and I. Mandel, Astrophys. J. **882**, 121 (2019).
[37] J. Veitch and A. Vecchio, Phys. Rev. D **81** (2010).
[38] I. M. Romero-Shaw *et al.*, Mon. Not. R. Astron. Soc. **499**, 3295 (2020).
[39] F. Acernese *et al.* (VIRGO Collaboration), Classical Quantum Gravity **32**, 024001 (2015).
[40] B. P. Abbott, R. Abbott, T. D. Abbott, M. Abernathy, F. Acernese, K. Ackley, C. Adams, T. Adams, P. Addesso, R. X. Adhikari *et al.*, Classical Quantum Gravity **34**, 104002 (2017).
[41] G. Ashton *et al.*, Astrophys. J. Suppl. **241**, 27 (2019).
[42] R. Smith, G. Ashton, A. Vajpeyi, and C. Talbot, Mon. Not. R. Astron. Soc. **498**, 4492 (2020).
[43] J. S. Speagle, Mon. Not. R. Astron. Soc. **493**, 3132 (2020).
[44] R. J. E. Smith, I. Mandel, and A. Vecchio, Phys. Rev. D **88**, 044010 (2013).
[45] G. Pratten, S. Husa, C. Garcia-Quiros, M. Colleoni, A. Ramos-Buades, H. Estelles, and R. Jaume, Phys. Rev. D **102**, 064001 (2020).
[46] C. García-Quirós, M. Colleoni, S. Husa, H. Estellés, G. Pratten, A. Ramos-Buades, M. Mateu-Lucena, and R. Jaume, Phys. Rev. D **102**, 064002 (2020).
[47] LIGO Scientific Collaboration, LIGO Algorithm Library—LALSuite, free software (GPL) (2020).
[48] G. Pratten *et al.*, Phys. Rev. D **103**, 104056 (2021).
[49] J. Lange, R. O'Shaughnessy, and M. Rizzo, arXiv: 1805.10457.
[50] R. J. E. Smith, I. Mandel, and A. Vechhio, Phys. Rev. D **88**, 044010 (2013).
[51] B. S. Sathyaprakash and B. F. Schutz, Living Rev. Relativity **12**, 2 (2009).
[52] R. Abbott *et al.*, Phys. Rev. X **11**, 021053 (2021).
[53] T. Dal Canton, S. Bhagwat, S. Dhurandhar, and A. Lundgren, Classical Quantum Gravity **31**, 015016 (2014).
[54] J. C. Bustillo, F. Salemi, T. Dal Canton, and K. P. Jani, Phys. Rev. D **97**, 024016 (2018).
[55] K. Chandra, V. Gayathri, J. C. Bustillo, and A. Pai, Phys. Rev. D **102**, 044035 (2020).
[56] I. Harry, J. Calderón Bustillo, and A. Nitz, Phys. Rev. D **97**, 023004 (2018).
[57] D. Gerosa and E. Berti, Phys. Rev. D **95**, 124046 (2017).
[58] M. Fishbach, D. E. Holz, and B. Farr, Astrophys. J. Lett. **840**, L24 (2017).
[59] E. Berti and M. Volonteri, Astrophys. J. **684**, 822 (2008).
[60] M. Pürrer and C.-J. Haster, Phys. Rev. Research **2**, 023151 (2020).
[61] V. Varma and P. Ajith, Phys. Rev. D **96**, 124024 (2017).
[62] J. Calderón Bustillo, S. Husa, A. M. Sintes, and M. Pürrer, Phys. Rev. D **93**, 084019 (2016).
[63] J. C. Bustillo, P. Laguna, and D. Shoemaker, Phys. Rev. D **95**, 104038 (2017).
[64] C. Capano, Y. Pan, and A. Buonanno, Phys. Rev. D **89**, 102003 (2014).
[65] T. B. Littenberg, J. G. Baker, A. Buonanno, and B. J. Kelly, Phys. Rev. D **87**, 104003 (2013).
[66] J. Calderón Bustillo, P. Laguna, and D. Shoemaker, Phys. Rev. D **95**, 104038 (2017).
[67] D. A. Brown, P. Kumar, and A. H. Nitz, Phys. Rev. D **87**, 082004 (2013).
[68] V. Varma, P. Ajith, S. Husa, J. C. Bustillo, M. Hannam, and M. Pürrer, Phys. Rev. D **90**, 124004 (2014).
[69] P. B. Graff, A. Buonanno, and B. S. Sathyaprakash, Phys. Rev. D **92**, 022002 (2015).
[70] C. Kalaghatgi, M. Hannam, and V. Raymond, Phys. Rev. D **101**, 103004 (2020).
[71] P. Kumar, J. Blackman, S. E. Field, M. Scheel, C. R. Galley, M. Boyle, L. E. Kidder, H. P. Pfeiffer, B. Szilagyi, and S. A. Teukolsky, Phys. Rev. D **99**, 124005 (2019).
[72] T. Islam, S. E. Field, C.-J. Haster, and R. Smith, Phys. Rev. D **103**, 104027 (2021).
[73] F. H. Shaik, J. Lange, S. E. Field, R. O'Shaughnessy, V. Varma, L. E. Kidder, H. P. Pfeiffer, and D. Wysocki, Phys. Rev. D **101**, 124054 (2020).
[74] S. E. Woosley, Astrophys. J. **836**, 244 (2017).
[75] M. Mapelli, N. Giacobbo, E. Ripamonti, and M. Spera, Mon. Not. R. Astron. Soc. **472**, 2422 (2017).
[76] M. Mapelli, M. Spera, E. Montanari, M. Limongi, A. Chieffi, N. Giacobbo, A. Bressan, and Y. Bouffanais, Astrophys. J. **888**, 76 (2020).
[77] U. N. Di Carlo, M. Mapelli, Y. Bouffanais, N. Giacobbo, F. Santoliquido, A. Bressan, M. Spera, and F. Haardt, Mon. Not. R. Astron. Soc. **497**, 1043 (2020).
[78] R. Cotesta, S. Marsat, and M. Pürrer, Phys. Rev. D **101**, 124040 (2020).